

# Tracking and motion analysis of the left ventricle with deformable superquadrics

Eric Bardinet<sup>1\*</sup>, Laurent D. Cohen<sup>2</sup> and Nicholas Ayache<sup>1</sup>

<sup>1</sup>CEREMADE, URA CNRS 749, Universite Paris IX - Dauphine, Place du Marechal de Lattre de Tassigny 75775 Paris CEDEX, France

<sup>2</sup>INRIA Sophia Antipolis, 2004 Route des Lucioles, B.P. 93, 06902 Sophia Antipolis CEDEX, France

## Abstract

We present a new approach to analyse the deformation of the left ventricle of the heart based on a parametric model that gives a compact representation of a set of points in a 3-D image. We present a strategy for tracking surfaces in a sequence of 3-D cardiac images. Following tracking, we then infer quantitative parameters which characterize: left ventricle motion, volume of left ventricle, ejection fraction, amplitude and twist component of cardiac motion. We explain the computation of these parameters using our model. Experimental results are shown in time sequences of two modalities of medical images, nuclear medicine and X-ray computed tomography (CT). Video sequences presenting these results are on the CD-ROM.

**Keywords:** Parametric models, tracking, left ventricle motion, quantitative analysis of motion

Received February 5, 1996; revised June 12, 1996; accepted August 20, 1996

## 1. INTRODUCTION

The analysis of cardiac deformations has given rise to a large amount of research in medical image understanding. Indeed, cardiovascular diseases are the primary cause of mortality in developed countries. Various imaging techniques (Acharya *et al.*, 1995) allow the acquisition of dynamic sequences of 3-D images (3-D+T) during a complete cardiac cycle (contraction and dilation). These images are well-suited to studying the behaviour of the cardiac system since they visualize how the heart wall deforms. Processing these images opens numerous fields of applications, such as detection and analysis of pathologies.

Advanced techniques of 3-D imagery, such as nuclear medicine and X-ray computed tomography (CT) provide ever increasing resolution in space and time. Consequently, the data available to the radiologist are becoming larger. However, to establish a reliable and fast diagnosis, the physician needs models that are defined by only a small number of characteristic quantities. A parametric deformable model allows the representation of a dynamic set of points by a

reasonable number of useful parameters, as we shall see below.

Since the left ventricle motion and deformation is an indication of the health of the heart, their study has been addressed by a number of research groups.

- The left ventricle reconstruction was done with generic deformable surface models (Ayache *et al.*, 1989; Cohen, 1991; Leitner and Cinquin, 1991; Cohen *et al.*, 1992b; Cohen and Cohen, 1993; Ayache *et al.*, 1994) but also with surface models dedicated to the left ventricle shape (Duncan *et al.*, 1991b; Amini and Duncan, 1992; Clarysse *et al.*, 1995).
- The left ventricle tracking was also studied with generic deformable surface models (Pentland and Horowitz, 1991; Ayache *et al.*, 1992; McInerney and Terzopoulos, 1995) and with the help of curvature information (Amini *et al.*, 1991; Duncan *et al.*, 1991a; Cohen *et al.*, 1992a; Friboulet *et al.*, 1993; Benayoun *et al.*, 1994; Benayoun *et al.*, 1995). Four dimensional models have been proposed by Shi *et al.* (1994) and Nastar and Ayache (1996) and the exploitation of temporal constraints was studied by Meyer *et al.* (1995) and McEachen *et al.* (1995).

\*Corresponding author  
(e-mail: bard@sophia.inria.fr)

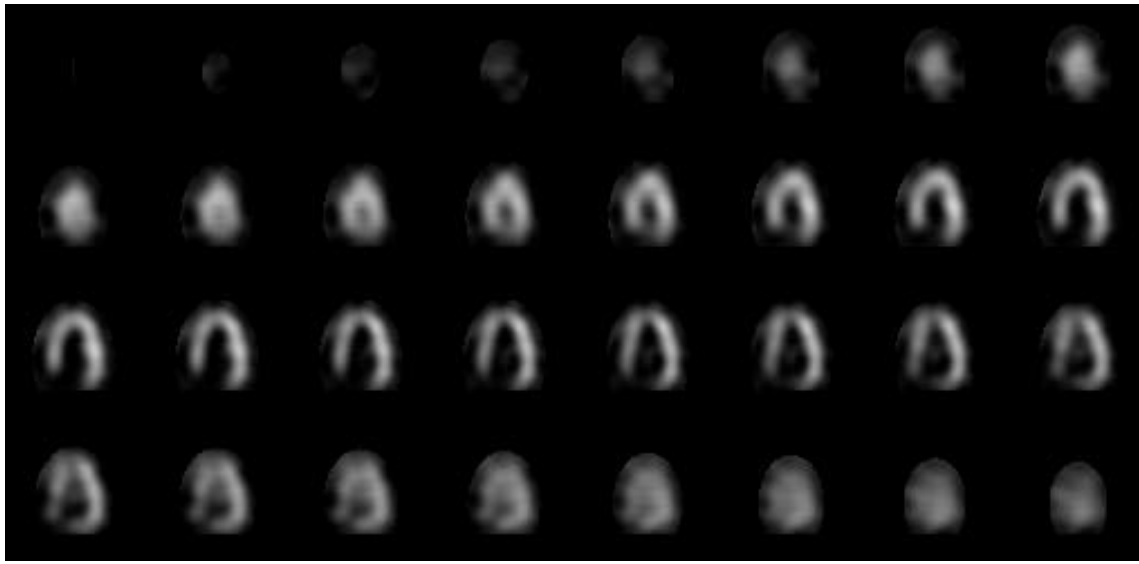


**Figure 1.** 3-D image of the left ventricle - SPECT image (the order of sections reads from left to right and from top to bottom). Dynamic presentation in the video.

- Finally, the extraction of parameters which capture the overall deformation was presented by Duncan *et al.* (1991a), Shi *et al.* (1995), Benayoun *et al.* (1995) and Nastar and Ayache (1996).
- In some images, some sparse ‘anchor points’ can be produced within the image to help the tracking process. This is the case of MRI-SPAMM images, and a number of studies take advantage of their properties (Amini *et al.*, 1994; Guttman *et al.* 1994; Young *et al.*, 1994; Kumar and Goldgof, 1994; Park *et al.*, 1996).

In a previous article (Bardinet *et al.*, 1996a), we introduced a parametric deformable model based on a superquadric fit followed by a free form deformation (FFD). The advantage of parametric deformable models like superquadrics is the small number of parameters needed to describe a shape combined with a better robustness in the presence of noise or sparse data. Also, at the expense of a reasonable number of additional parameters, FFDs provide a close fit and a volumetric deformation estimation.

In the present article, we first give a summary of our segmentation algorithm, specific to cardiac images, in Section 2. In Section 3, we briefly summarize the results of Bardinet *et al.* (1996a) on the parametric model, necessary for a good understanding of this article. In Section 4, we present an approach to track surfaces with this model in a sequence of 3-D images, and give experimental results for tracking the deformation of the left ventricle in two different kinds of

3-D medical images. In Section 5, we explain how to infer, from the parametric reconstruction, a number of quantitative parameters useful to characterize the left ventricle motion. We demonstrate the feasibility of the approach on two kinds of temporal sequences of 3-D images. We believe that the results are sufficiently promising to initiate a thorough clinical validation.

## 2. SEGMENTATION OF CARDIAC IMAGES

We studied two different kinds of images.

- Nuclear medicine data, the SPECT sequence, with eight successive time frames during one cardiac cycle. Each image is a volume of  $64 \times 64 \times 64$  voxels (volume of the voxel:  $1.446 \text{ mm}^3$ ), describing a human heart.
- X-ray CT data, the DSR (dynamic spatial reconstructor) sequence, with 18 successive time frames during one cycle. Each image is a volume of  $98 \times 100 \times 110$  voxels (volume of the voxel:  $0.926 \text{ mm}^3$ ), describing a canine heart.

The original 3-D images are visualized as a series of 2-D cross-sections in Figures 1 and 3.

We first have to extract a set of points belonging to the endocardium (the inner surface of the left ventricle) and/or to the epicardium (the outer surface of the left ventricle). These points will be then approximated by a deformable superellipsoid in the next section. In DSR images, a single

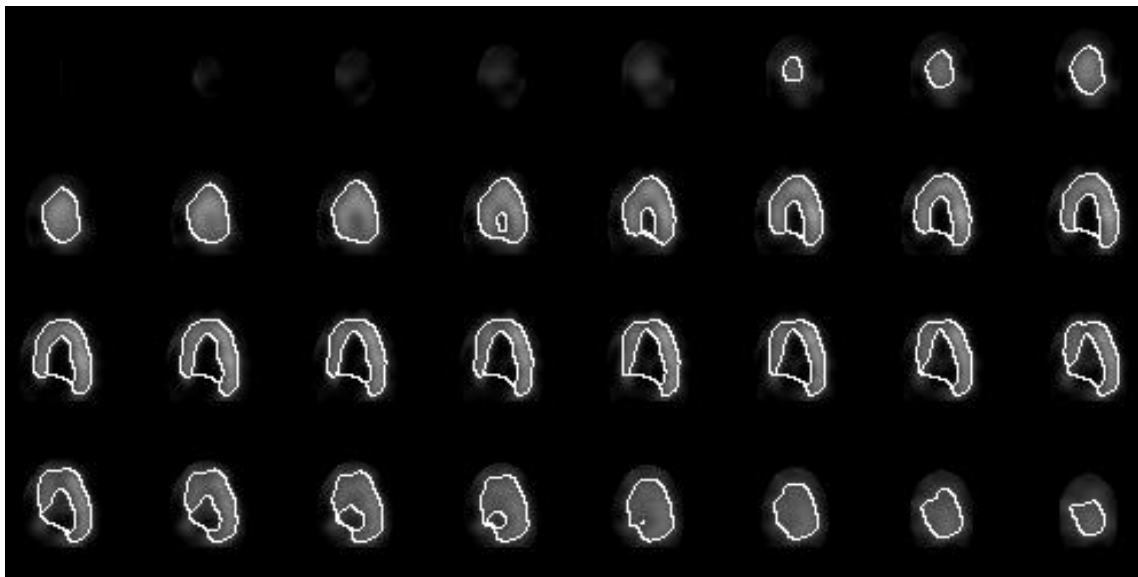


**Figure 2.** Segmentation of the epicardium and the endocardium (external and internal surfaces of the left ventricle) on the SPECT image (the order of sections reads from left to right and from top to bottom). Dynamic presentation in the video.

threshold is sufficient to isolate the left ventricle cavity, and therefore extract the endocardium. On the other hand, the epicardium is not sufficiently well-contrasted to be robustly extracted. In the SPECT images, it is possible to extract grossly the epicardium and endocardium surfaces with a threshold based on the histogram of the intensities (Goris and Bertille, 1992). Then, with the help of mathematical morphology operators (Serra, 1982; Höhne and Hanson, 1992), we automatically smooth and isolate both surfaces.

Therefore, in the following, we assume that we have extracted the points belonging respectively either to the endocardium (DSR and SPECT images) and/or to the epicardium (SPECT images only). Although extracting surfaces from the SPECT sequence seems to be a difficult task, let us point out that we ran experiments successfully on six SPECT sequences with the same segmentation process. Results of the segmentation processes on the two data sequences are presented in Figures 2 and 4 for data at time step 1, and in Figures 6 and 8 for one cross-section over time during the sequence. For a correct estimation of the quality of those segmentations, we superimposed the segmented surface(s) on the image.

### 3. A PARAMETRIC MODEL TO FIT 3-D DATA

In this section, we briefly describe the deformable model that we use to represent the inner and outer surfaces of the left ventricle [a detailed presentation is in Bardinet *et al.* (1996a)].

We refine our superquadric model using a parametric deformation. More precisely, for a given set of 3-D points (we have seen in the previous section how get from the 3-D images of the heart a number of 3-D points belonging to the inner or outer surfaces of the left ventricle), we first fit 3-D data with a superellipsoid, and then refine this crude approximation using free form deformations (FFDs).

#### 3.1. Fitting 3-D data with superquadrics

Superquadric shapes have been widely used in vision and graphics. In computer vision, their first use is due to Pentland (1987), followed by Solina and Bajcsy (1990) who used superellipsoids to approximate 3-D objects. The goal of the algorithm is to find a set of parameters such that the superellipsoid best fits the set of data points. Superquadrics form a family of implicit surfaces obtained by extension of conventional quadrics. Superellipsoids centered at the origin and with principal axes corresponding to the reference axes are defined by the implicit equation:

$$\left( \left( \left( \frac{x}{a_1} \right)^{2/\epsilon_2} + \left( \frac{y}{a_2} \right)^{2/\epsilon_2} \right)^{\epsilon_2/\epsilon_1} + \left( \frac{z}{a_3} \right)^{2/\epsilon_1} \right)^{\epsilon_1/2} = 1, \quad (1)$$

which involves five independent parameters. To generate a superellipsoid centered at an arbitrary location and with an arbitrary orientation of its principal axes, we must add the six parameters of a rigid displacement, which makes 11 parameters required for an arbitrary superellipsoid. Suppose

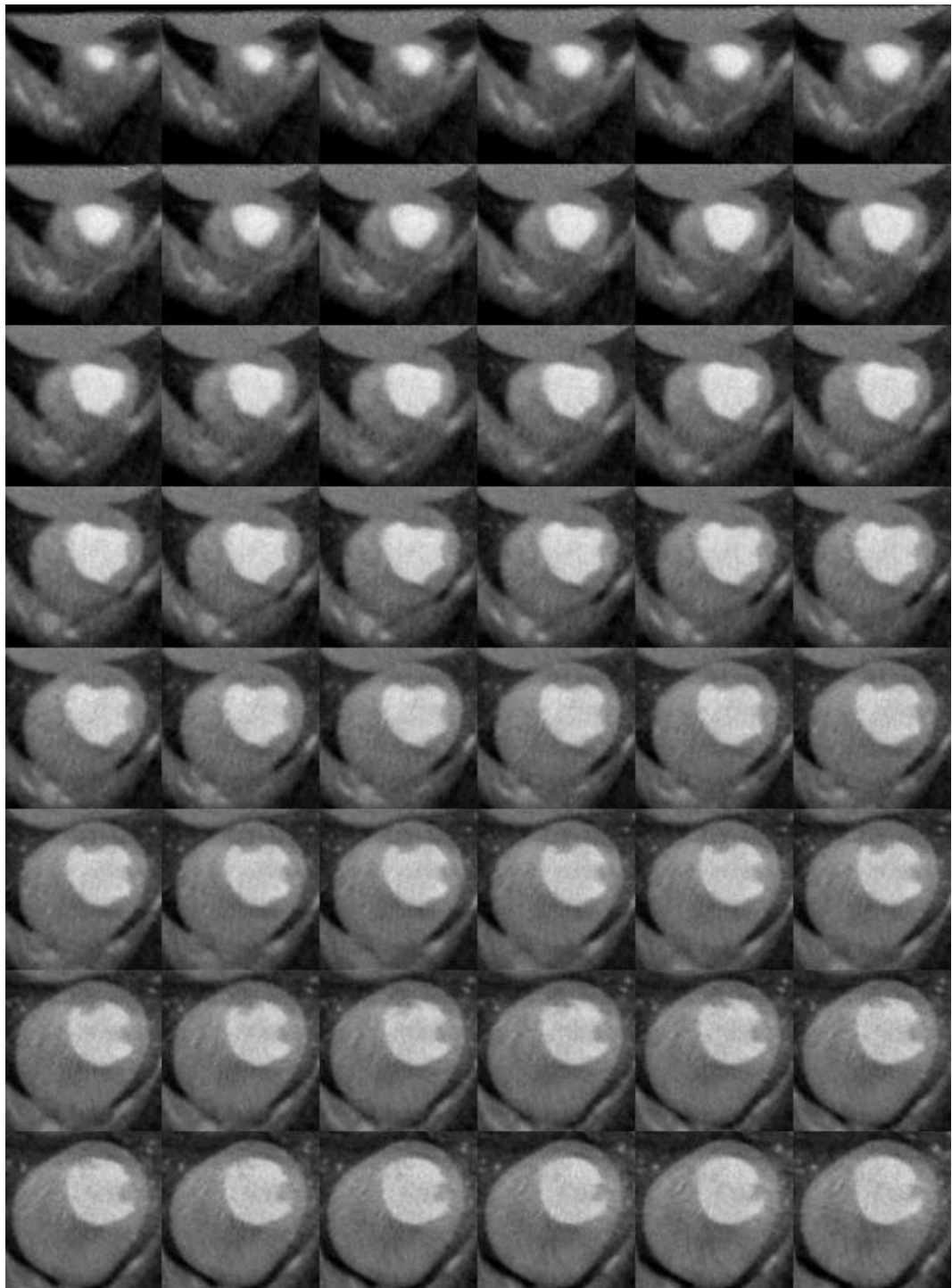


**Figure 3.** 3-D image of the left ventricle - DSR image (the order of sections reads from left to right and from top to bottom).

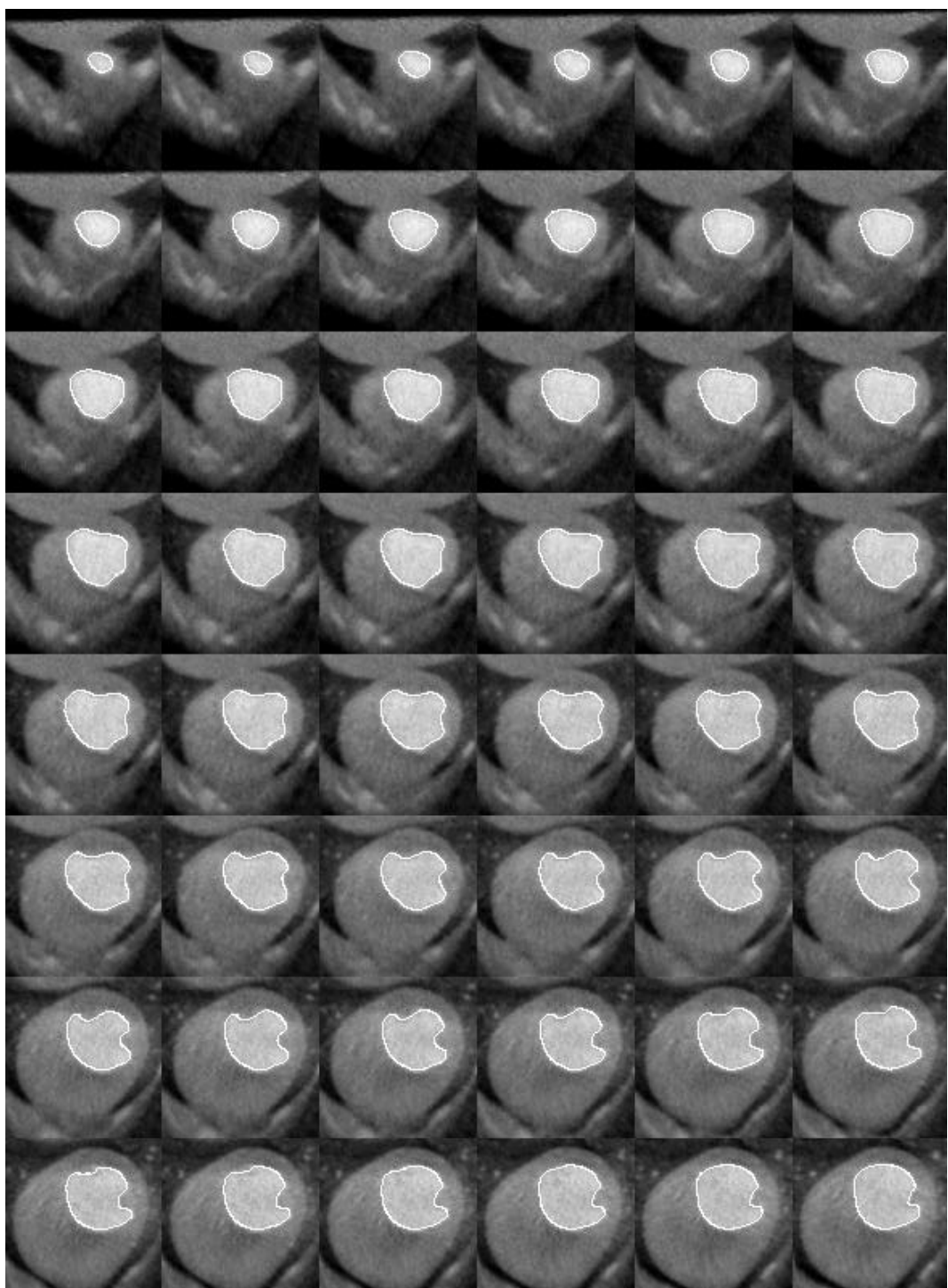


**Figure 4.** Segmentation of the endocardium (internal surface of the left ventricle) on the DSR image (the order of sections reads from left to right and from top to bottom).

that the data we want to fit with the superellipsoid are a set of 3-D points  $(x_i, y_i, z_i)$ ,  $i = 1, \dots, N$ . Since a point on the surface of the superellipsoid satisfies  $F = 1$ , where  $F$  is the function defined by Equation (1), we find the minimum of the following energy:

$$E(A) = \sum_{i=1}^N [1 - F(x_i, y_i, z_i, A)]^2, \quad (2)$$

where  $A$  denotes the set of 11 parameters needed to describe the superellipsoid [see Bardinet *et al.* (1996a) for details about the minimization technique used and also for a geometric interpretation of this energy].

### 3.2. Refinement with free form deformations

We now refine this parametric representation of the 3-D data, using a global volumetric deformation called FFD. This is a tool devoted to the deformation of solid geometric models in a free-form manner [see Sederberg and Parry (1986)]. The main interest of FFDs is that the resulting deformation of the object, although potentially complex, is defined by a small number of points. This characteristic feature allows us to represent voluminous 3-D data by a model defined by a relatively small number of parameters (11 parameters + 125 points).

#### 3.2.1. Definition of FFDs

FFDs were introduced by Sederberg and Parry (1986) in computer graphics and have been used to solve matching problems by Szeliski and Lavallée (1994). An FFD is a mapping from  $\mathbb{R}^3$  to  $\mathbb{R}^3$ , defined by the tensor product of trivariate Bernstein polynomials. The principle of FFDs is as follows: the object to be deformed is embedded in a 3-D box. Inside this box, a volumetric grid of points is defined, which links the box to the object (by the trivariate polynomial which defines the deformation function):

$$\begin{aligned} \mathbf{X} = & \sum_{i=0}^l \sum_{j=0}^m \sum_{k=0}^n C_l^i C_m^j C_n^k (1-s)^{l-i} s^i \\ & \times (1-t)^{m-j} t^j (1-u)^{n-k} u^k \mathbf{P}_{ijk}, \end{aligned} \quad (3)$$

where  $\mathbf{P}_{ijk}$  denotes the volumetric grid of control points,  $(s, t, u)$  denotes the local coordinates of the object points in a frame defined by the box of control points and  $(l, m, n)$  denotes the degrees of the Bernstein polynomials. This can be written in a matrix form:  $\mathbf{X} = \mathbf{B}\mathbf{P}$ , where  $\mathbf{B}$  is the deformation matrix  $N_d \times N_p$  ( $N_d$  is the number of points on the discretized superellipsoid and  $N_p$  is the number of control points of the grid),  $\mathbf{P}$  is a matrix  $N_p \times 3$  which contains the coordinates of the control points and  $\mathbf{X}$  is a matrix  $N_d \times 3$  with the coordinates of the model points. The box is then deformed by the displacement of its lattice, and the position of a point of

**Table 1.** Typical computation times with an increasing number of control points of the FFD for 20 iterations.

Size of the FFD	Computation time (s)
$2 \times 2 \times 2 = 8$	243
$3 \times 3 \times 3 = 27$	244
$4 \times 4 \times 4 = 64$	265
$5 \times 5 \times 5 = 125$	429
$6 \times 6 \times 6 = 216$	751

the deformed object is computed [see Bardinet *et al.* (1996a) for details].

#### 3.2.2. The inverse problem

We need to solve the inverse problem: first compute a initial displacement field  $\delta\mathbf{X}$  between the superellipsoid and the data and then, after having put the superellipsoid in a 3-D box, search for the deformation  $\delta\mathbf{P}$  of this box which will best minimize the displacement field  $\delta\mathbf{X}$ :

$$\min_{\delta\mathbf{P}} \|\mathbf{B}\delta\mathbf{P} - \delta\mathbf{X}\|^2 \quad (4)$$

This is illustrated in Figure 5.

In practice, we use an iterative two-step algorithm [see Bardinet *et al.* (1996a) for details], similar to the formulation of B-spline snakes with auxiliary variables, as described in Cohen (1995).

The current displacement field  $\delta\mathbf{X}$  is computed after a set of matches is established between the image data points and the current position of the model (which is a deformed superellipsoid after the first iteration). In our implementation, a data point is matched with the closest model point, but other strategies, involving for instance the local curvature, could be successfully applied (Duncan *et al.*, 1991a; Amini *et al.*, 1991; Cohen *et al.*, 1992a; Ayache *et al.*, 1992; Shi *et al.*, 1994; Benayoun *et al.*, 1994; Feldmar and Ayache, 1994; Benayoun *et al.*, 1995).

We use boxes of size  $5 \times 5 \times 5$  for data sets of  $\sim 6,000$  points, and the number of iterations is between 10 and 30. Therefore we get an average compression ratio of 46 [computed as  $(6000 \times 3)/(125 \times 3 + 11)$ , where 11 is the number of parameters needed for the superellipsoid (compare with Subsection 3.1)]. This number of parameters provides a reasonable trade-off between approximation quality and computation time. Table 1 presents typical computation times of the FFD with 20 iterations and different sizes for the box of control points (on a DEC Alpha 300).

#### 3.2.3. Simultaneous deformation of two surfaces

An essential feature of this algorithm is that FFD is a volumetric deformation. This means that several objects can

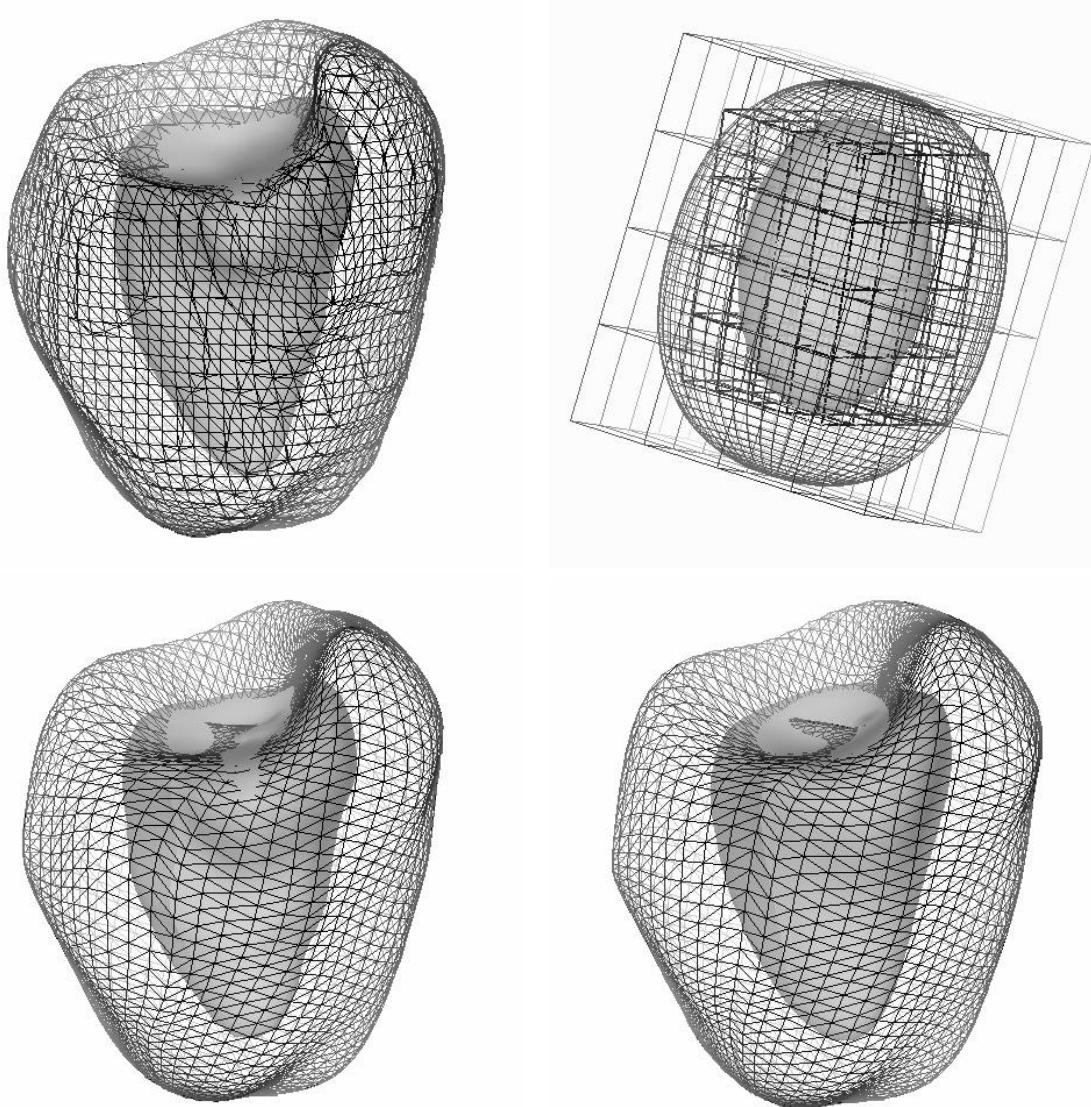


**Figure 5.** Deformation of two surfaces. Top left: data: epicardium (mesh) and endocardium (rendered surface) described respectively with 4500 and 1500 points. Top right: two fitted superellipsoids and the two initial boxes of control points. Bottom left: final models obtained with two FFDs (each defined by 11 parameters + 125 points). Compression ratio: 23. Bottom right: simultaneous deformation of the two superellipsoids with only one FFD (defined by 11 parameters + 125 points). Compression ratio: 46.

be simultaneously deformed with only one FFD. Using only one model means that the two surfaces are put in a same box of control points and the minimization of Equation (4) is done simultaneously based on the union of the two displacement fields.

Figure 5 shows the result of the algorithm for the reconstruction of the epicardium and the endocardium from the SPECT data with two superellipsoids deformed first by two

independent FFDs, and then by a single common FFD (in this last case, the unique box of control points is the largest one, i.e. the one computed for the epicardium). The corresponding approximation errors for the SPECT data, computed as the averages of errors between the data and the final model (projecting each 3-D data point onto the deformed model), are presented in Table 2. One can see that using two FFDs for the two surfaces leads to a better quality of approximation.

**Table 2.** Averages of errors between original data and parametric models for SPECT data (in mm).

	Separate computation	Simultaneous computation	Precision loss %
Epicardium	0.097590	0.102623	5.2
Endocardium	0.128125	0.135583	5.8

Left column, each model is computed independently; middle column, the two models are computed with one FFD; right column, computation with only one FFD leads to a slight loss of the approximation precision.

On the other hand, using only one FFD allows to divide the number of parameters by two, yielding a larger compression of the information needed for the description of the parametric model.

#### 4. TRACKING OF THE LEFT VENTRICLE

Having extracted 3-D points corresponding to the wall of the left ventricle in a time sequence of images, we show in this section how we use our parametric model to make an efficient tracking of the LV wall in a sequence of 3-D images.

##### 4.1. Tracking strategy: recursive representation with a unique deformation

Our strategy is the following: the complete model (superellipsoid + FFD) is fitted only to the surfaces of the left ventricle extracted in the first image. Then, a unique FFD (which is now a deformed box of control points) is used with a new displacement field computed between the previous model and the data of the next image, and so on for the complete sequence. Finally, the models at any time are defined by only one FFD applied to a single original superellipsoid.

Following the formulation of Subsection 3.2.2, the model at time  $n$ ,  $\mathbf{X}_n$ , can be written:

$$\mathbf{X}_n = \mathbf{B}_0 (\mathbf{P}_0 + \delta\mathbf{P}_0^* + \cdots + \delta\mathbf{P}_{n-1}^*) , \quad (5)$$

where  $\delta\mathbf{P}_i^*$  is the increment in the position of control points at iteration  $i$  which minimizes the error defined in Subsection 3.2.2 between the deformed model and the extracted surface(s) of the left ventricle.

One can notice that this strategy requires the inversion of a linear system of the form  $\mathbf{X} = \mathbf{BP}$  only once [by computing the pseudoinverse of the matrix with a singular value decomposition, see Bardinet *et al.* (1996a) for details], thus tracking of a sequence is quite efficient.

##### 4.2. Experimental results on cardiac images

We present in this section results of the tracking algorithm on the cardiac images described in Section 2.

Figure 6 shows the dynamic SPECT sequence on a particular cross-section ( $z = 32$ ), with the segmented and

reconstructed surfaces superimposed (see Section 2). It also shows the reconstruction of these two surfaces using either one or two models as explained in Subsection 3.2.3. Figure 7 presents the same results for the 3-D rendering of the surface.

Figure 8 shows the dynamic DSR sequence on a cross-section, first the original image, then the segmented endocardium surface superimposed (see Section 2) and also the reconstruction of this surface with the parametric model. Figure 9 depicts the same result for the 3-D rendering of the surface for three time steps of the sequence. Table 3 shows the CPU time for each complete time sequence (on a DEC Alpha 300).

All these results are also presented in the video attached to this article (see Appendix C).

#### 5. QUANTITATIVE ANALYSIS OF LEFT VENTRICLE DEFORMATION

The reconstruction and representation of a time sequence of surfaces by a sequence of parametric models allows to visualize the estimation of the deformation through time. More precisely, the parametric representation provides a way to determine the motion field on the cardiac wall. This motion field can then be used to extract some characteristic parameters useful for the diagnosis.

Let us here point out that these parameters are deduced from a geometrical representation of the left ventricle motion. Thus, the question we have to keep in mind is the following: what kind of parameters are of interest for the physician? There are parameters which he already uses for diagnosis, and he is familiar with, so that he can assess the practicability of the model. In the area of cardio-vascular diseases, and especially in the study of the cardiac muscle, an important parameter is the volume of the left ventricle, as well as its temporal evolution, which permits to compute the ejection fraction (ratio characterizing the ‘pumping’ nature of the heart). This is the content of Subsection 5.1.

We also present other types of parameters. These ones are not yet used for diagnosis, and a complete clinical validation is clearly required to assess their usefulness.

In Subsection 5.2, we present parameters that can be deduced from the trajectories of parametric points of the model

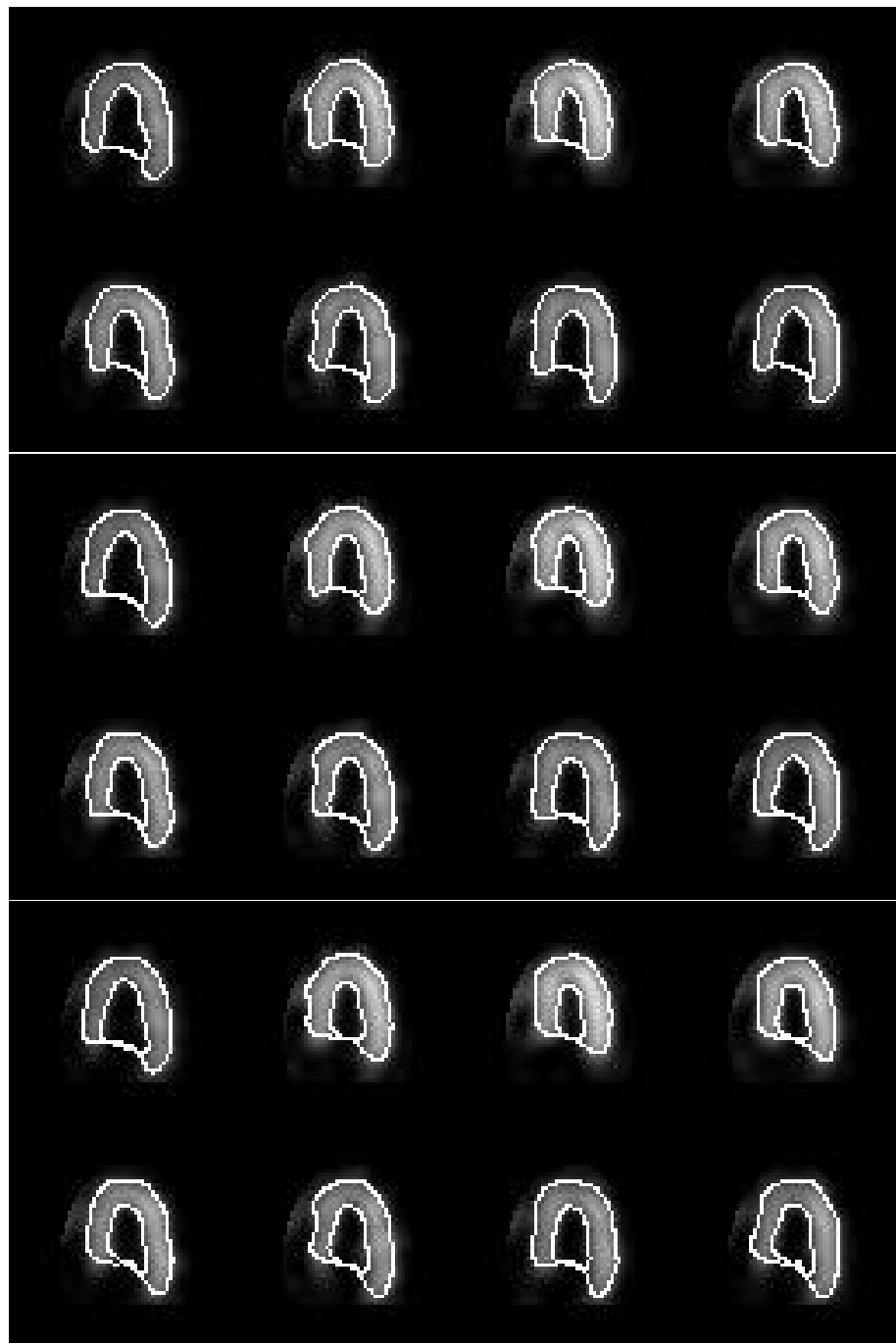


**Figure 6.** Segmentation and representation of the epicardium and the endocardium for a time sequence (3-D+T) of the left ventricle during the cardiac cycle - SPECT image; visualization of a cross-section over time. Top: segmented surfaces superimposed on the image. Middle: approximation by 2 independent deformable superellipsoids (2 FFDs). Bottom: approximation by 2 coupled deformable superellipsoids (1 FFD).

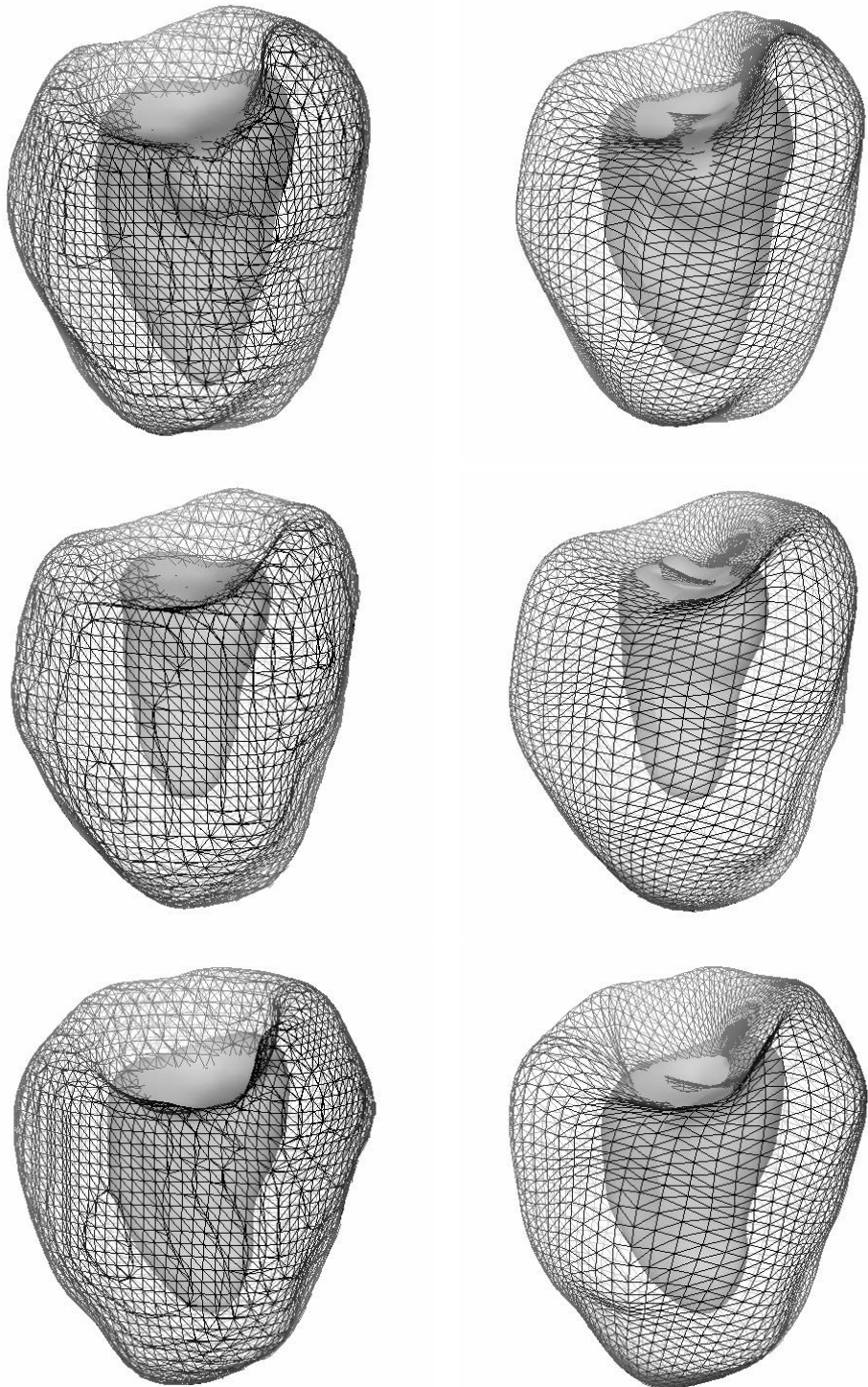


**Figure 7.** Time sequence of the epicardium (mesh) and the endocardium (rendered surface) ( $t = 1, 3, 5$ ) SPECT images. Left: isosurfaces obtained by data segmentation (4500 + 1500 points). Right: representation by two parametric models ( $2 \times (11 \text{ parameters} + 125 \text{ points})$ ). Dynamic presentation in the video.

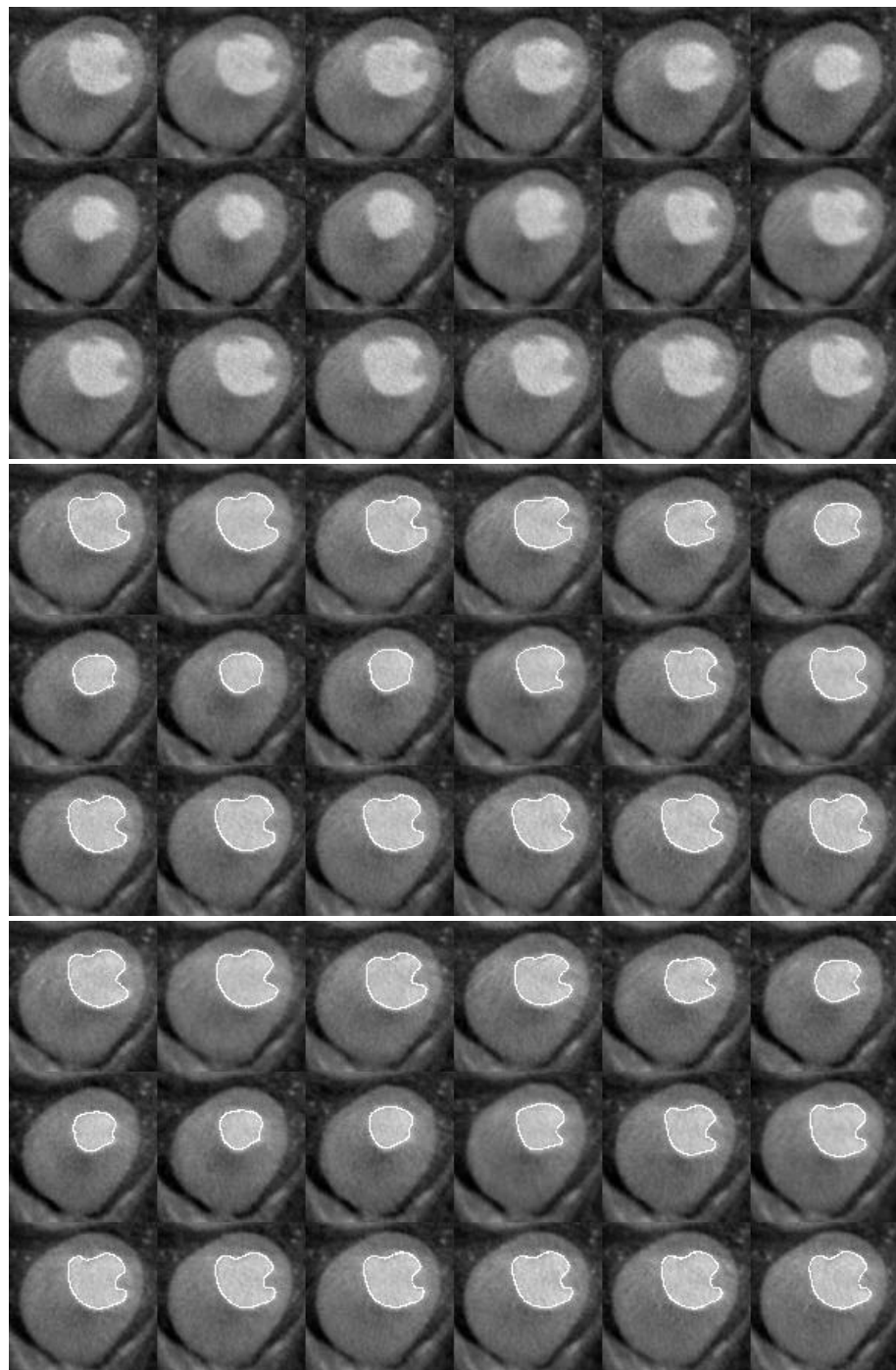


**Figure 8.** A cross-section over time, during a cardiac cycle (DSR). Top: original image. Middle: segmentation. Bottom: reconstruction with a deformable superellipsoid involving 11 parameters + 125 points.

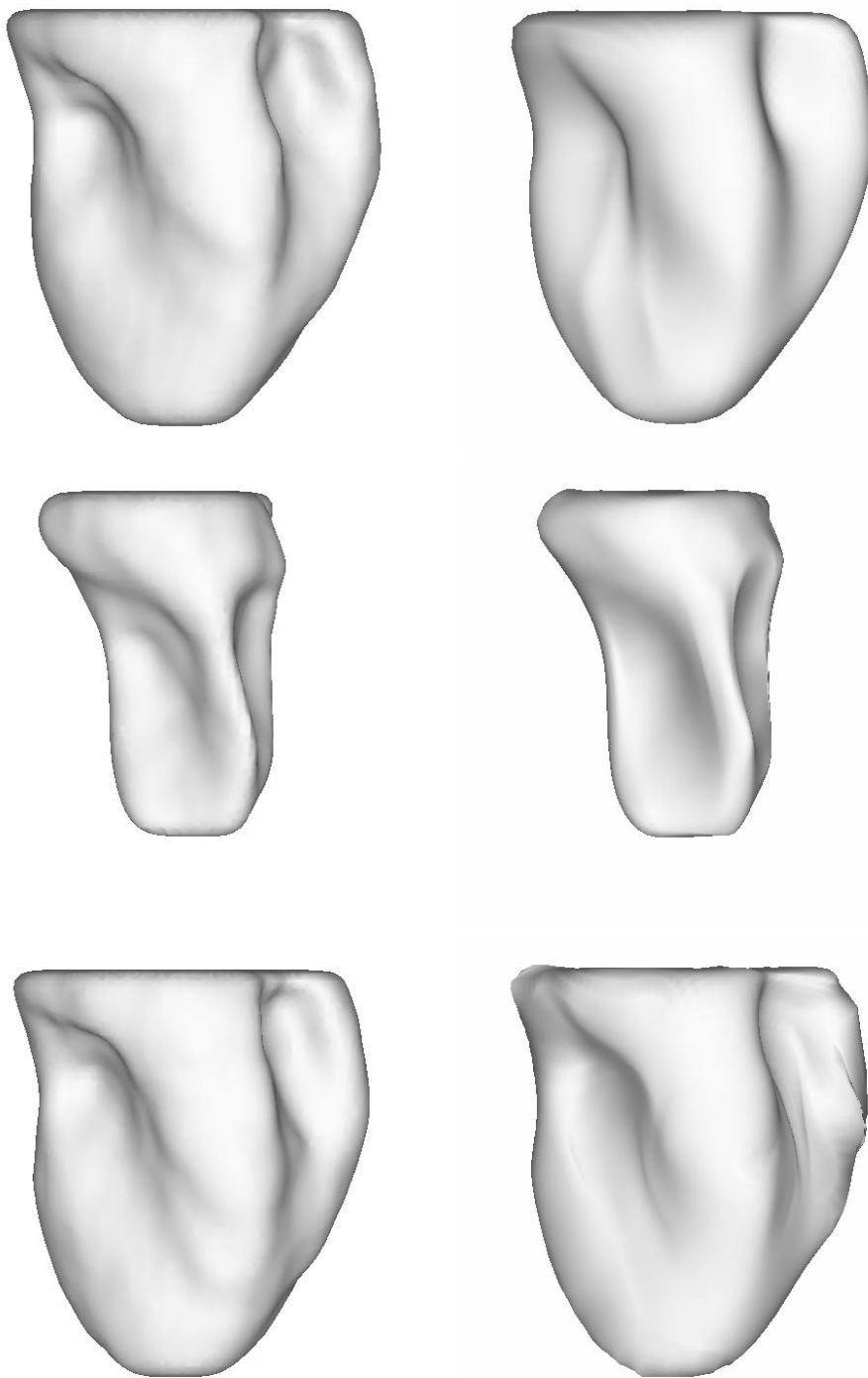


**Figure 9.** Time sequence of the endocardium ( $t = 1, 8, 13$ ) DSR images. Left: isosurfaces obtained by segmentation (10000 points). Right: reconstruction by the parametric model defined by 11 parameters + 125 points (DSR). Compression ratio: 77.

**Table 3.** Tracking the complete DSR and SPECT sequences: number of points (FFD and model), number of iterations, number of time frames and computation times.

	FFD	Model	Iterations	Frames	Computation time (min)
SPECT	125	2500	10	8	25
DSR	125	5000	10	18	72

during a cardiac cycle: amplitude and twist component of the motion, temporal evolution of the left ventricle wall thickness.

### 5.1. Volume evolution

To evaluate the ejection fraction, we need to compute the temporal evolution of the left ventricle volume. We first calculate an explicit form of the volume of a superellipsoid, depending on its parameters, and then show how to calculate the volume of a polyhedral region bounded by a mesh of vertices, using the discrete form of the Gauss integral theorem.

#### 5.1.1. Volume of a superellipsoid

Let  $S$  be a superellipsoid surface defined by the following implicit equation:

$$\left( \left( \frac{x}{a_1} \right)^{\frac{2}{\epsilon_2}} + \left( \frac{y}{a_2} \right)^{\frac{2}{\epsilon_2}} \right)^{\frac{\epsilon_2}{\epsilon_1}} + \left( \frac{z}{a_3} \right)^{\frac{2}{\epsilon_1}} = 1. \quad (6)$$

Its volume can be explicitly computed by using the following formula:

$$V = 2 a_1 a_2 a_3 \epsilon_1 \epsilon_2 \beta \left( \frac{\epsilon_2}{2}, \frac{\epsilon_2}{2} + 1 \right) \beta \left( \frac{\epsilon_1}{2}, \epsilon_1 + 1 \right)$$

(see Appendix A for details).

#### 5.1.2. Volume inside a mesh

Considering an oriented mesh defined by a set of points and a set of faces, the volume inside the mesh can be written:

$$V = \sum_{i=1}^K V_i = \frac{1}{3} \sum_{i=1}^K (OM, N) S_i, \quad (7)$$

where  $K$  is the number of faces of the mesh,  $O$  is a reference point,  $M$  is a point on the mesh and  $N$  is the normal vector at  $M$ , pointing outwards.

This expression can be rewritten:

$$V = \frac{1}{6} \sum_{i=1}^K (OG, N_d),$$

where  $N_d$  and  $G$  denote respectively the normal vector and the barycenter of a face (see Appendix B for details).

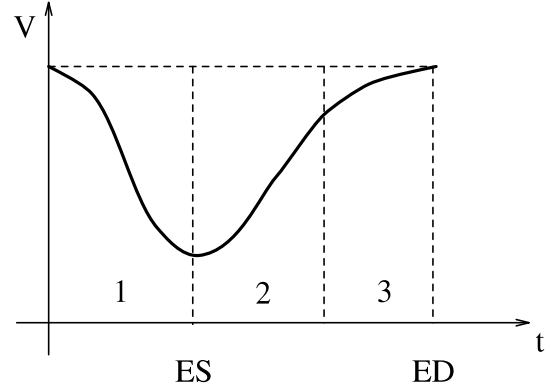


**Figure 10.** Typical shape of the temporal evolution of ventricular volume. The curve is divided into 3 parts: 1. Fast contraction 2. Fast dilation 3. Slow dilation.

#### 5.1.3. Discussion

We applied this calculation of epicardium and endocardium volumes to the sequences of both data points and parametric models obtained in the previous sections. Once we have computed the values of the volume along a cardiac cycle, we can easily obtain the ejection fraction [calculated precisely as:  $\frac{Vd - Vc}{Vd}$ , with  $Vd$  volume at dilation (the end of diastole),  $Vc$  volume at contraction (the end of systole), see for example Davis *et al.* (1993)]. The results presented in Figure 11 show the following.

- The evolution of the volume has the expected typical shape found in the medical literature (Goris and Bretille, 1992) and shown in Figure 10. Moreover, the estimation of the ejection fraction on our example gives a value of 68%, which is in the range of expected values (Goris and Bretille, 1992; Davis *et al.*, 1993).
- The volumes computed on the data points or on the deformable superellipsoids are almost equal. The relative average absolute error along the cycle is 0.42%. This proves that our model is robust with respect to the volume estimation. Of course, the ejection fraction is also obtained with a very small relative error (0.19%).
- The volume evolution found for initial superellipsoid models before FFD, has also a very similar shape, as seen in Figure 11. However, there is a size ratio due to

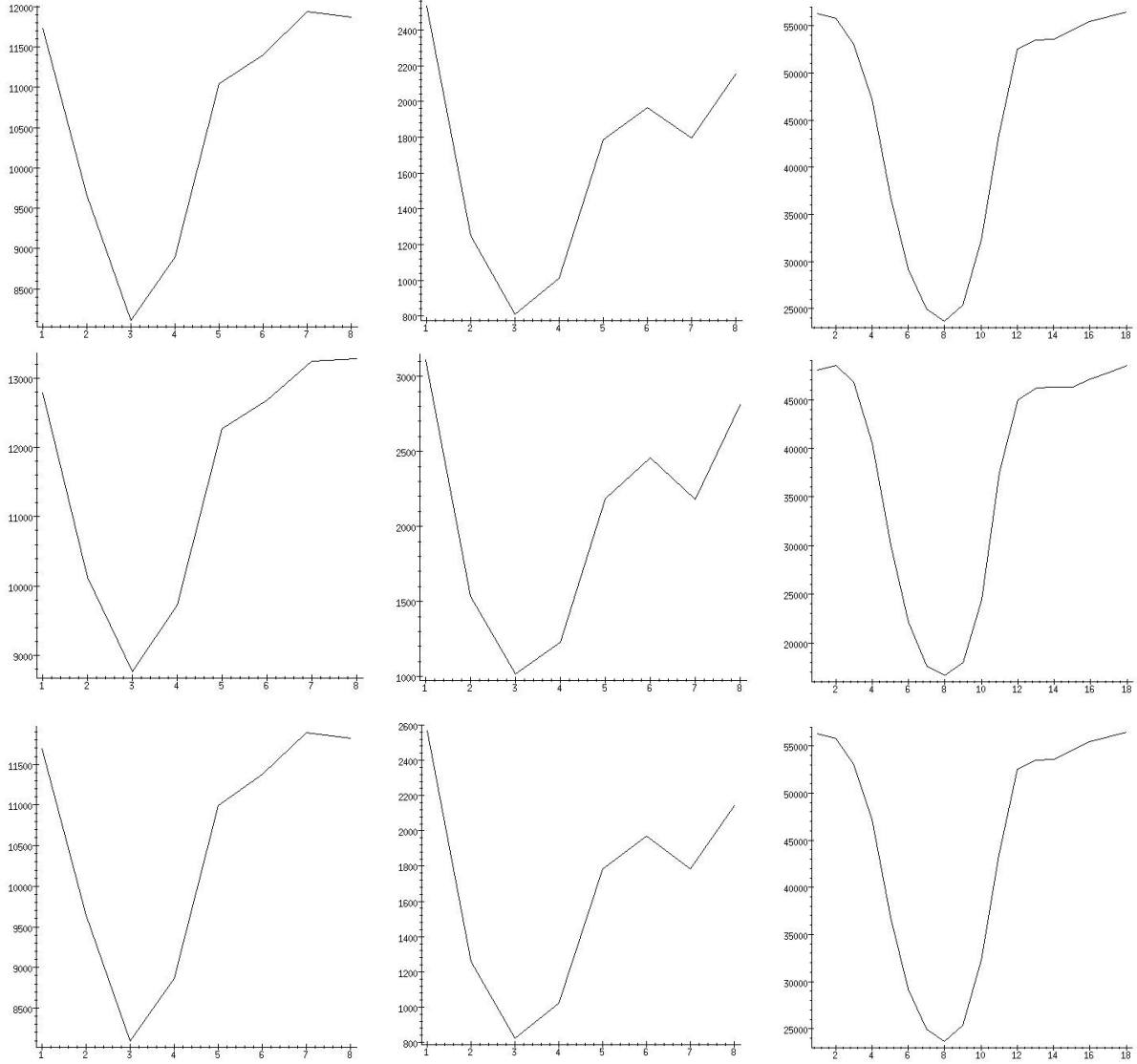


**Figure 11.** Cardiac volumes during the cardiac cycle. Left: volumes of the epicardium (SPECT). Middle: volumes of the endocardium (SPECT). Right: volumes of the endocardium (DSR). Top row: volumes computed on the data points. Middle row: volumes of the superellipsoids. Bottom row: volumes of the deformable superellipsoids. Note that the relative average absolute errors between the volumes of the deformable superellipsoids and the segmented data along the cycle are less than 1%.

the over-estimation of the volume before the FFD. This ratio is almost constant through time, which makes it possible to get a good estimate of the ejection fraction directly from the initial model. This proves that the superellipsoid model provides a good global estimate of the shape. Also, the volume of the superellipsoid can be obtained analytically from its set of parameters without the previous discrete approximation (see Sub-section 5.1.1).

## 5.2. Trajectories

Listing the successive positions of a parametric point of the deformed surface model along the time sequence, we obtain the trajectory followed by this point.

### 5.2.1. Decomposition into cylindrical coordinates

The decomposition of the model points trajectories into cylindrical coordinates (see Figure 12) will allow us to compute two interesting parameters: twist component of the motion

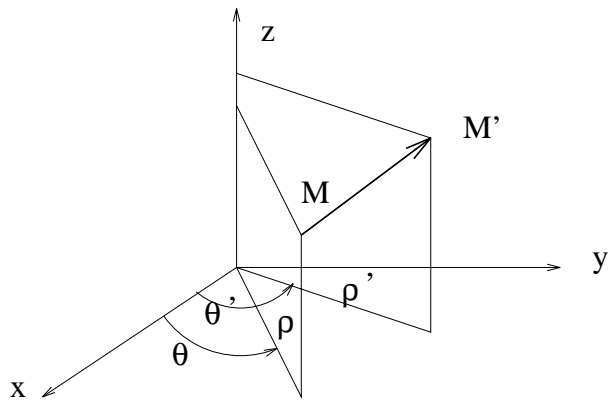


**Figure 12.** Cylindrical coordinates of two points  $M$  and  $M'$ , which represent the same parametric point at the beginning and at the end of the cardiac cycle.

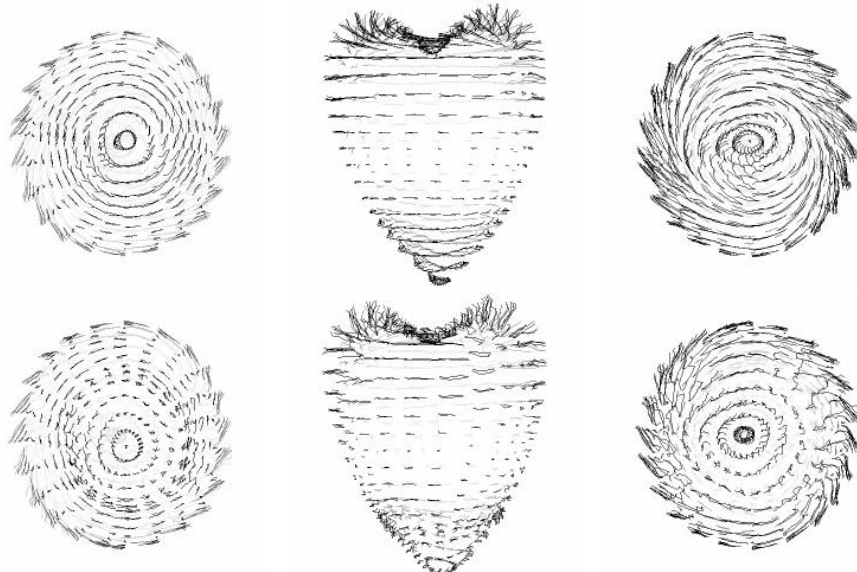


**Figure 13.** Trajectories on a synthetic example. Top: original trajectories. Bottom: estimated trajectories. Left column: view from the apex. Middle column: front view. Right column: view from the base. Dynamic presentation in the video.

and temporal evolution of the wall thickness.

$$\begin{pmatrix} x \\ y \\ z \end{pmatrix} \rightarrow \begin{pmatrix} \rho &= \sqrt{x^2 + y^2} \\ \theta &= \arccos\left(\frac{x}{\sqrt{x^2 + y^2}}\right) \\ z &= z \end{pmatrix} \quad (8)$$

We will consider, as frame of reference of the cylindrical representation, the frame of reference of the superellipsoid fitted to the segmented data at the first step of the time sequence.

To measure the twist, we compute the difference of the  $\theta$  parameters for the two points that represent the same parametric point during the contraction.

The wall thickness is computed as the difference of the  $\rho$  parameters for two corresponding parametric points on the epicardium and the endocardium [correspondences can be established by different criteria: in a preliminary study, we used the parametric values on the original superellipsoids, before the application of FFDs, see Bardinet *et al.*, (1996b) for details, but this will be improved in a future work].

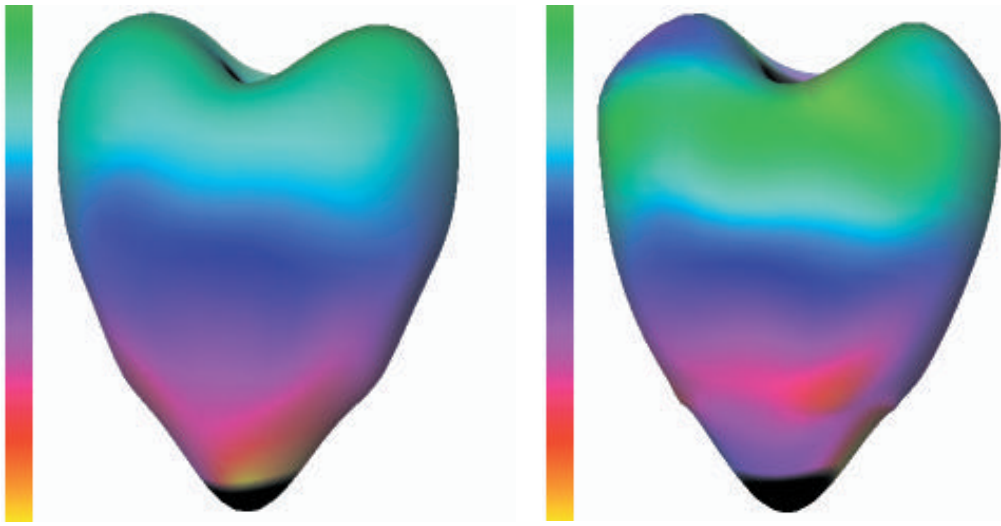


**Figure 14.** Twist component estimation on a synthetic example. Left: actual values. Right: estimated values (see text).

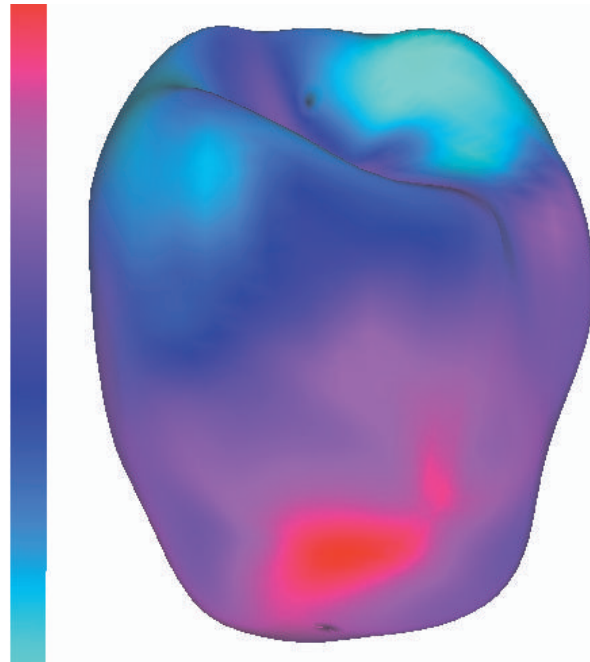


**Figure 16.** Amplitude of motion computed at each model point during a cardiac contraction (SPECT). Dynamic presentation in the video.

### 5.2.2. Synthetic example

To get a precise idea of the capability of the model in recovering a twist motion, we studied a synthetic example.

First, we define a sequence of parametric surfaces representing a synthetic heart during a complete cardiac cycle (17 successive time frames). All the models of this sequence are

obtained with the following implicit equation:

$$\left( \left( \frac{x}{a_1} \right)^2 + \left( \frac{y}{a_2} \right)^2 + \left( \frac{z}{a_3} \right)^2 \right)^3 - \left( c_1 \left( \frac{x}{a_1} \right)^2 + c_2 \left( \frac{y}{a_2} \right)^2 \right) \left( \frac{z}{a_3} \right)^3 = 1,$$

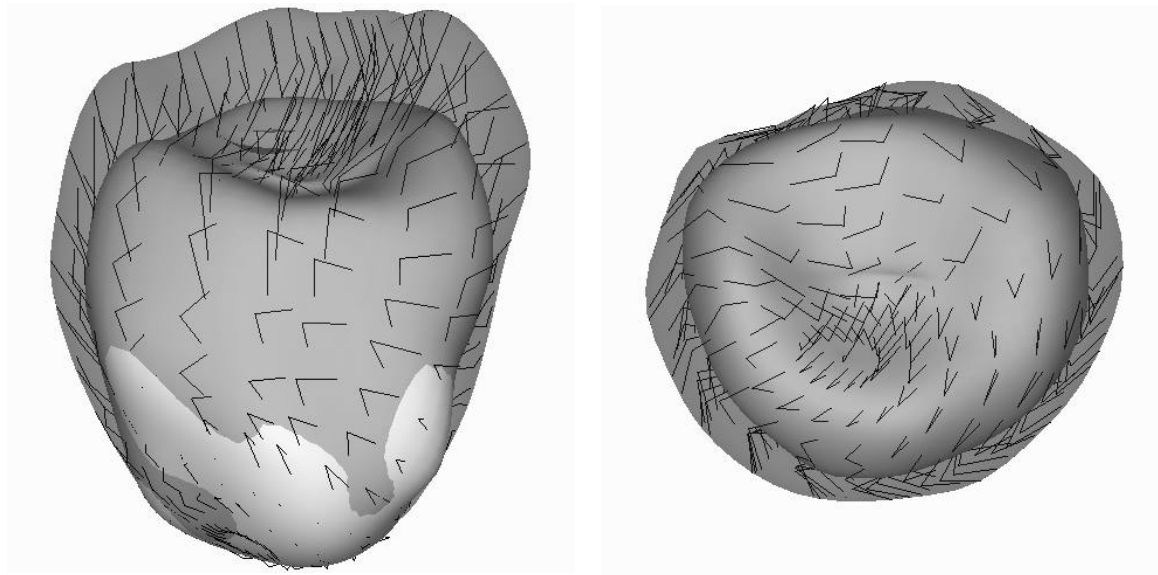


**Figure 15.** Trajectories of points on the model of the epicardium during the systolic stage (contraction, during three successive time frames) from two viewpoints (SPECT). The two surfaces represent the deformable superellipsoids respectively at the beginning and end of systole. Dynamic presentation in the video.

where  $a_1 = 10$ ,  $a_2 = 12$ ,  $a_3 = 14$  and  $c_1$  and  $c_2$  are periodic temporal functions to simulate a gross beating motion (a more sophisticated model would have included a translation of the origin and a rotation of the principal axes). The complete sequence is computed with the following 17 values of  $c_1$ : 3.3, 2.9, 2.5, 2.3, 2.1, 1.9, 1.7, 1.5, 1.7, 1.9, 2.1, 2.3, 2.5, 2.7, 2.9, 3.1, 3.3 (same values for  $c_2$ ).

Starting from this sequence, we add a global axial twist around the z-axis of the models, as defined by Barr (1984):

$$\begin{aligned} \theta &= f(z) \\ C_\theta &= \cos(\theta), \quad S_\theta = \sin(\theta) \end{aligned}$$

$$\left\{ \begin{array}{l} X = xC_\theta - yS_\theta \\ Y = xS_\theta + yC_\theta \\ Z = z \end{array} \right.$$

$f$  is defined as follows: the angle  $\theta$  varies linearly from  $\alpha$  on the apex to  $-\alpha$  on the base, with  $\alpha$  varying along the sequence from  $0^\circ$  up to  $30^\circ$ , then back to  $0^\circ$ . A very recent work (Wakes *et al.*, 1996) presents a cardiac motion simulator, which could yield a more sophisticated synthetic example.

We then try to recover the known trajectories using our tracking strategy. Recovering a twist motion is a difficult problem, since the displacement of each point has a tangential component which cannot be easily detected. Figure 13 presents the recovered trajectories compared with the original ones.

One can see (and this is particularly visible in the attached video) that the tracking method provides results which are close to the original trajectories, and catch the twist component of the motion. This is probably due to the discrete nature of the synthetic example, which forces the ‘closest’ match on the second surface to include a tangential component. With real data, either tags or curvature attributes would be required to obtain a similar result.

Figure 14 represents the values of this twist, where a colour has been associated to the twist value for each model point, on the original synthetic data and for the models recovered by the tracking method.

### 5.2.3. Real images

Figure 15 show the estimated trajectories on the epicardium surface during the systolic stage for the SPECT data. These are visualized from different viewpoints to appreciate better the motion, and also in the video attached to this article (see Appendix C).

The pointwise tracking of the deformation allows an evaluation of the motion field during the sequence. The visualization of these displacements using different colour values on the surface clearly shows those areas on the ventricle where the displacements are small (see Figure 16).

## 6. CONCLUSION

We have presented a new approach to analyse the deformation of the heart left ventricle with a parametric model. It is based on a parametric model that gives a compact representation of a set of points in a 3-D image. We have presented a method which efficiently tracks the left ventricle wall in a sequence of 3-D images during a cardiac cycle using this model and studied synthetic and real data. The model is able to track simultaneously the endocardium and the epicardium, since it is a volumetric deformation.

It is then possible to compute the variation of the volume during a cardiac cycle and the ejection fraction. We showed on a synthetic example that it might also be possible to estimate the twist component in the deformation of the ventricle, provided that some local features allow for the recovery of the tangential component of the motion.

Future directions will include the clinical evaluation of this work, and also its adaptation to MRI-SPAMM images where we could use our model to track and interpolate a smooth deformation between tagged points.

## 7. ACKNOWLEDGEMENTS

We would like to thank Grégoire Malandain who contributed to the segmentation of the images presented in this article; and Jérôme Declerck, Serge Benayoun and Alexis Gourdon for constructive remarks; many thanks also to Lewis Griffin and Allen Sanderson for their careful reviews of this article, and to the reviewers of this article for their numerous and relevant remarks. The images of the SPECT sequence were supplied by Prof. Michael Goris, from Stanford University. Thanks to Dr Rich Robb and Dennis P. Hanson of Biomedical Imaging Resource, Mayo Foundation/Clinic for the DSR data. This work was partially supported by Digital Equipment Corporation.

## REFERENCES

- Acharya, R., Wasserman, R., Stevens, J. and Hinojosa, C. (1995) Biomedical imaging modalities: a tutorial. *Comput. Med. Imag. Graphics*, 19, 3–25.
- Amini, A. and Duncan, J. (1992) Bending and stretching models for LV wall motion analysis from curves and surfaces. *Image Vision Comput.*, 10, 418–430.
- Amini, A., Owen, R., Anandan, P. and Duncan, J. (1991) Non-rigid motion models for tracking the left ventricular wall. In Information Processing in Medical Images, *Lecture Notes in Computer Science*, 511, pp. 343–357. Springer-Verlag.
- Amini, A., Curwen, R., Constable, R. and Gore, J. (1994) MR physics-based snake tracking and dense deformations from tagged cardiac images. In *AIII Spring Symposium Series: Applications of Computer Vision in Medical Image Processing*, Austin, TX, pp. 126–129.
- Ayache, N., Boissonnat J. D., Brunet, E., Cohen, L., Chièze, J. P., Geiger, B., Monga, O., Rocchisani, J. M. and Sander, P. (1989) Building highly structured volume representations in 3D medical images. *Proceedings Computer Assisted Radiology*. Springer, Berlin.
- Ayache, N., Cohen, I. and Herlin, I. (1992) In Blake, A. and Yuille, A. (eds), *Active Vision*. Springer, Berlin, pp. 285–302.
- Ayache, N., Cinquin, P., Cohen, I., Cohen, C., Leitner, F. and Monga, O. (1994) In Taylor, R., Lavallée, S., Burdea, G. and Mösges, R. (eds), *Computer-Integrated, Surgery*. MIT Press, MA, pp. 59–74.
- Bardinet, E., Cohen, L. and Ayache, N. (1996a) A parametric deformable model to fit unstructured 3D data. *Comput. Vision Image Understanding*, in press (also INRIA RR-2617, available by anonymous ftp at ftp.inria.fr /INRIA/tech-reports/RR/).
- Bardinet, E., Cohen, L. and Ayache, N. (1996b) *Analyzing the deformation of the left ventricle of the heart with a parametric deformable model*. INRIA RR-2797 (available by anonymous ftp at ftp.inria.fr /INRIA/tech-reports/RR/).
- Barr, A. (1984) Global and local deformations of solid primitives. *Computer Graphics* (SIGGRAPH'84), 18, 21–30.
- Benayoun, S., Ayache, N. and Cohen, I. (1994) Adaptive meshes and nonrigid motion computation. In *Int. Conf. on Pattern Recognition*, Jerusalem, Israel, October.
- Benayoun, S., Nastar, C. and Ayache, N. (1995) Dense non-rigid motion estimation in sequences of 3D images using differential constraints. In *Conf. on Computer Vision, Virtual Reality and Robotics in Medicine*, Nice, France, April, *Lecture Notes in Computer Science*, 905, pp. 309–318. Springer-Verlag.
- Clarysse, P., Poupon, F., Barbier, B. and Magnin, I. (1995) 3-D boundary extraction of the left ventricle by a deformable model with a priori information. In *IEEE Int. Conf. on Image Processing*, October.
- Cohen, L. (1991) On active contour models and balloons. *Computer Vision, Graphics, and Image Processing: Image Understanding*, 53, 211–218.
- Cohen, L. (1995) Auxiliary variables and two-step iterative algorithms in computer vision problems. *J. Math. Imag. Vision*, 6, 61–86.
- Cohen, I., Ayache, N. and Sulger, P. (1992a) Proceedings ECCV'92, Ligure, Italy, May. *Lecture Notes in Computer Science*, 588. Springer, Berlin.
- Cohen, I., Cohen, L. and Ayache, N. (1992b) Using deformable surfaces to segment 3-D images and infer differential structures. *Computer Vision, Graphics, and Image Processing: Image Understanding*, 56, 242–263.
- Cohen, L. and Cohen, I. (1993) Finite element methods for active contour models and balloons for 2-D and 3-D images. *IEEE Trans. PAMI*, 15, 1131–1147.
- Davis, M., Rezaie, B. and Weiland, F. (1993) Assessment of left ventricular ejection fraction from technetium-99m-methoxy isobutyl isonitrile multiple-gated radionuclide angiocardiography. *IEEE Trans. Med. Imag.*, 12, 189–199.

- Declerck, J., Feldmar, J. and Ayache, N. (1996) Definition of a 4D continuous polar transformation for the tracking and the analysis of LV motion. INRIA RR, in preparation.
- Duncan, J., Owen, R., Staib, L. and Anandan, P. (1991a) Measurement of non-rigid motion using contour shape descriptors. *IEEE Comput. Soc. Comput. Vision Pattern Recognition*, pp. 318–324.
- Duncan, J., Lee, F., Smeulders, A. and Zaret, B. (1991b) A bending energy model for measurement of cardiac shape deformity. *IEEE Trans. Med. Imag.*, 10, 307–319.
- Feldmar, J. and Ayache, N. (1995) Rigid, affine and locally affine registration of free-form surfaces. *Int. J. Comput. Vision*, in press (see also INRIA RR-2220, available by anonymous ftp at <ftp://ftp.inria.fr/INRIA/tech-reports/RR/>).
- Friboulet, D., Magnin, I., Mathieu, C., Pommert, A. and Hoehne, K. (1993) Assessment and visualization of the curvature of the left ventricle from 3-D medical images. *Comput. Med. Imag. Graphics*, 17, 257–262.
- Goris, M. and Bretille, J. (1992) *A Colour Atlas of Nuclear Cardiology*. Chapman and Hall, London.
- Guttman, M., Prince, J. and McVeigh, E. (1994) Tag and Contour Detection in Tagged MR Images of the Left Ventricle. *IEEE Trans. Med. Imag.*, 13, 74–88.
- Höhne, K. and Hanson, W. (1992) Interactive 3D segmentation of MRI and CT volumes using morphological operations. *J. Comput. Assis. Tomogr.*, 16, 285–294.
- Kumar, S. and Goldgof, D. (1994) Automatic Tracking of SPAMM Grid and the Estimation of Deformation Parameters from Cardiac MR Images. *IEEE Trans. Med. Imag.*, 13, 122–132.
- Leitner, F. and Cinquin, P. (1991) EMBS '91. October 31–November 3, Orlando, FL.
- McEachen, J., Meyer, F., Constable, R., Nehorai, A. and Duncan, J. (1995) A recursive filter for phase velocity assisted shape-based tracking of cardiac non-rigid motion. *IEEE Int. Conf. on Computer Vision*, Cambridge, MA, United States, June, pp. 653–658. IEEE Computer Society Press.
- McInerney, T. and Terzopoulos, D. (1995) A dynamic finite element surface model for segmentation and tracking in multidimensional medical images with application to cardiac 4D image analysis. *Comput. Med. Imag. and Graphics*, 19, 69–83.
- Meyer, F., Constable, R., Sinusas, A. and Duncan, J. (1995) Tracking myocardial deformation using spatially-constrained velocities. *Proceedings of the 14th Int. Conf. 'Information Processing in Medical Imaging'*, Ile de Berder, France, June, pp. 177–188. Kluwer Academic, Dordrecht.
- Nastar, C. and Ayache, N. (1996) Frequency-based nonrigid motion analysis: application to 4 dimensional medical images. *IEEE Trans. PAMI*, in press (see also Spatio-temporal analysis of non-rigid motion from 4D data (1994) in IEEE Workshop on Motion of Nonrigid and Articulate Objects, available at <http://www-syntim.inria.fr/syntim/research/nastar/nastar-mnao94.ps.Z>).
- Park, J., Metaxas, D. and Axel, L. (1996) Analysis of left ventricular wall motion based on volumetric deformable models and MRI-SPAMM. *Med. Image Anal.*, 1, 53–71.
- Pentland, A. (1987) Recognition by parts. *IEEE Int. Conf. on Computer Vision*, pp. 612–620. IEEE Computer Society Press.
- Pentland, A. and Horowitz, B. (1991) Recovery of nonrigid motion and structure. *IEEE Trans. PAMI*, 13, 730–742.
- Sederberg, T. and Parry, S. (1986) Free-form deformation of solid geometric models. *Comput. Graphics (SIGGRAPH'86)*, 20, 151–160.
- Serra, J. (1982) *Image Analysis And Mathematical Morphology*, vol. 1. Academic Press, London.
- Shi, P., Amini, A., Robinson, G., Sinusas, A., Constable, C. and Duncan, J. (1994) Shape-based 4D left ventricular myocardial function analysis. *IEEE Workshop on Biomedical Image Analysis*, Seattle, June, pp. 88–97.
- Shi, P., Robinson, Constable, C., Sinusas, A. and Duncan, J. (1995) A model-based integrated approach to track myocardial deformation using displacement and velocity constraints. *IEEE Int. Conf. on Comput. Vision*, Cambridge, MA, June, pp. 687–692. IEEE Computer Society Press.
- Solina, F. and Bajcsy, R. (1990) Recovery of parametric models from range images: the case for superquadrics with global deformations. *IEEE Trans. PAMI*, 12, 131–147.
- Szeliski, R. and Lavallée, S. (1994) Matching 3-d anatomical surfaces with non-rigid deformations using octree-splines. In *IEEE Workshop on Biomedical Image Analysis*, Seattle, June, pp. 144–153.
- Waks, E., Prince, J. and Douglas, A. (1996) Cardiac motion simulator for tagged MRI. *IEEE Workshop on Mathematical Methods in Biomedical Image Analysis*, pp. 182–191.
- Young, A., Kraitchman, D. and Axel, L. (1994) Deformable Models for Tagged MR Images: Reconstruction of 2- and 3-Dimensional Heart Wall Motion. In *IEEE Workshop on Biomedical Image Analysis*, Seattle, June, pp. 317–323.

## APPENDICES

### A. CALCULATION OF THE VOLUME OF A SUPERELLISSOID

Let  $S$  be a superellipsoid surface defined by the following implicit equation:

$$\left( \left( \frac{x}{a_1} \right)^{\frac{2}{\epsilon_2}} + \left( \frac{y}{a_2} \right)^{\frac{2}{\epsilon_2}} \right)^{\frac{\epsilon_2}{\epsilon_1}} + \left( \frac{z}{a_3} \right)^{\frac{2}{\epsilon_1}} = 1. \quad (9)$$

An explicit parameterization of  $S$  is given by:

$$\begin{cases} x &= a_1 \cos^{\epsilon_1} \eta \cos^{\epsilon_2} \omega, & -\frac{\pi}{2} \leq \eta \leq \frac{\pi}{2} \\ y &= a_2 \cos^{\epsilon_1} \eta \sin^{\epsilon_2} \omega, & -\pi \leq \omega < \pi \\ z &= a_3 \sin^{\epsilon_1} \eta \end{cases}$$

Due to the symmetry of the surface in relation to the 3 axes of the coordinate system, the computation of the volume inside  $S$  can be made as follows:

$$V = 2 \int_0^{a_3} A(z) dz, \quad (10)$$

where  $A(z)$  is the area of a slice among the z-axis. For  $\eta = 0$ , the implicit equation of the corresponding slice is:

$$\left(\frac{x}{a_1}\right)^{\frac{2}{\epsilon_2}} + \left(\frac{y}{a_2}\right)^{\frac{2}{\epsilon_2}} = 1$$

This leads to:

$$A(0) = 4 a_2 \int_0^{a_1} y(x) dx = 4 a_2 \int_0^{a_1} \left(1 - \left(\frac{x}{a_1}\right)^{\frac{2}{\epsilon_2}}\right)^{\frac{\epsilon_2}{2}} dx$$

Setting:  $X = \left(\frac{x}{a_2}\right)^{\frac{2}{\epsilon_2}}$ , it becomes:

$$A(0) = 2 a_1 a_2 \epsilon_2 \beta\left(\frac{\epsilon_2}{2}, \frac{\epsilon_2}{2} + 1\right),$$

where  $\beta(x, y)$  denotes the Beta function (Euler's integral of the first kind):

$$\beta(x, y) = \int_0^1 t^{x-1} (1-t)^{y-1} dt$$

Finally, to calculate the volume inside  $S$  using Equation 10, we have to write  $a_1$  and  $a_2$  as functions of  $z$ . From the implicit definition of  $S$  (Equation 9), we deduce:

$$\begin{aligned} a_1(z) &= a_1 \left(1 - \left(\frac{z}{a_3}\right)^{\frac{2}{\epsilon_1}}\right)^{\frac{\epsilon_1}{2}}, \\ a_2(z) &= a_2 \left(1 - \left(\frac{z}{a_3}\right)^{\frac{2}{\epsilon_1}}\right)^{\frac{\epsilon_1}{2}} \end{aligned}$$

Therefore:

$$V = 2 \int_0^{a_3} 2 \epsilon_2 \beta\left(\frac{\epsilon_2}{2}, \frac{\epsilon_2}{2} + 1\right) a_1(z) a_2(z) dz$$

Setting:  $Z = \left(\frac{z}{a_3}\right)^{\frac{2}{\epsilon_1}}$ , it becomes:

$$V = 2 a_1 a_2 a_3 \epsilon_1 \epsilon_2 \beta\left(\frac{\epsilon_2}{2}, \frac{\epsilon_2}{2} + 1\right) \beta\left(\frac{\epsilon_1}{2}, \epsilon_1 + 1\right)$$

Note that for a sphere ( $\epsilon_1 = \epsilon_2 = 1$ ,  $a_1 = a_2 = a_3 = R$ ), the previous formula gives:

$$V = 2 R^3 \beta\left(\frac{1}{2}, \frac{3}{2}\right) \beta\left(\frac{1}{2}, 2\right) = \frac{4}{3} \pi R^3$$

## B. CALCULATION OF THE VOLUME INSIDE A MESH

Let  $D$  be a region of space with bounding surface  $\partial D$ ; the unit normal vector  $n$  to  $\partial D$  is drawn outwards. Then:

$$\int \int \int_D \frac{\partial u(x, y, z)}{\partial x} dx dy dz = \int \int_{\partial D} u \cos(n, x) dS \quad (11)$$

(and similarly for  $y$  and  $z$ ). Equation 11 holds under very general assumptions:  $u$  must be continuous in  $D$  and have continuous bounded first partial derivatives; the boundary surface  $\partial D$  must have continuously varying tangent planes, except at finitely many vertices and edges. From this equation, we obtain (among others) the following formula:

$$\int \int \int_D \operatorname{div} u = \int \int_{\partial D} u dS = \int \int_{\partial D} (u, n) dS,$$

known as the Gauss integral theorem, where  $\operatorname{div}(.)$  denotes the divergence of a vector field and  $(., .)$  denotes the scalar product in  $\mathbb{R}^3$ .

Let  $O$  be a reference point. Using this theorem, we can write:

$$\int \int \int_D \operatorname{div}(OM) dx dy dz = \int \int_{\partial D} (OM, n) dS,$$

where  $M$  is a point on  $\partial D$ . Now, it is obvious that the value of the divergence of the vector field  $OM$  is 3. Therefore, the Gauss integral theorem yields an expression of the volume inside a domain  $D$ :

$$V = \int \int \int_D dV = \frac{1}{3} \int \int_{\partial D} (OM, n) dS \quad (12)$$

Considering an oriented mesh defined by a set of points and a set of faces, the volume inside the mesh can be written, using the previous formula:

$$V = \sum_{i=1}^K V_i = \frac{1}{3} \sum_{i=1}^K (OM, N) S_i, \quad (13)$$

where  $K$  is the number of faces of the mesh.

We now have to define the normal vector of a face. Assuming that the face is defined by three points  $A_1$ ,  $A_2$  and  $A_3$ , the normal vector can be written:

$$N_d = (A_1 - A_2) \wedge (A_1 - A_3) = A_1 \wedge A_2 + A_2 \wedge A_3 + A_3 \wedge A_1,$$

where  $(. \wedge .)$  denotes the vector product. Note that the norm of this normal vector is linked to the surface  $S$  of the face as follows:  $\|N_d\| = 2S$ . One can easily generalize this formula for a face defined by a set of points  $A_i$ ,  $i = 1..M$ :

$$N_d = \sum_{i=1}^{M-1} (A_i \wedge A_{i+1}) + A_M \wedge A_1$$

This expression can be seen as the average of the normal vectors of the decomposition of the face into triangular subfaces.

Let suppose that the mesh is composed of triangular faces defined by  $A_1$ ,  $A_2$  and  $A_3$ . The volume  $V_i$  of the tetrahedron  $OA_1A_2A_3$  is:

$$V_i = \frac{S.H}{3},$$

where  $H$  is the height. Let  $O$  be the origin and  $G$  be the barycenter of a face. Then:

$$H = \frac{(OG, N_d)}{\|N_d\|}$$

And therefore:

$$V_i = \frac{(OG, N_d)}{6}$$

This last expression is still true for a face defined by  $M$  points.

Finally, Equation 13 can be rewritten:

$$V = \frac{1}{6} \sum_{i=1}^K (OG, N_d)$$

### C. CONTENT OF THE VIDEO

The video is consisting in six sequences:

1. Nuclear medicine data (SPECT image). The first image of the sequence is visualized as a series of 2-D cross-sections (transverse slices). See Section 2 for details (**0–20 s**).
2. Segmentation of the SPECT sequence. See Section 2 for details (**20–40 s**).
3. Tracking of the epicardium (mesh) and the endocardium (rendered surface) in the SPECT sequence; on the left, the segmented surfaces, on the right, the reconstructed models. See Sections 2 and 4.2 for details (**40 s–1 min**).
4. On the left, trajectories of the node points, on the right, velocity field in the SPECT sequence. See Subsection 5.2.3 for details (**1–1 min 20 s**).
5. Recovery of a twist motion on a synthetic example (1). Data with trajectories. See Subsection 5.2.2 for details (**1 min 20 s–1 min 40 s**).
6. Recovery of a twist motion on a synthetic example (2). Trajectories on the data and on the models computed with tracking method. See Subsection 5.2.2 for details (**1 min 40 s–2 min**).